Mapping Heat Flux

WALT MCKEOWN

Naval Research Laboratory, Oceanography Division, Remote Sensing Applications, Stennis Space Center, Mississippi

RICHARD LEIGHTON

Naval Research Laboratory, Washington, D.C.

(Manuscript received 21 November 1997, in final form 17 December 1997)

ABSTRACT

An infrared camera technique designed for remote sensing of air–water heat flux has been developed. The technique uses the differential absorption of water between 3.817 and 4.514 microns. This difference causes each channel's radiance to originate over a different range of depths inside the air–water interface temperature gradient. Since this gradient varies only with total heat flux, the radiance difference between channels caused by the gradient also varies with heat flux. Laboratory experiments showed that this radiance difference correlates well with heat flux measured independently with calorimetry. A regression relation between camera output and heat flux is determined initially using time variations of the radiance difference and heat flux. This relation is modified by a partial differential analysis of the relative contributions of temperature and heat flux using data from experiments designed for this evaluation. The result is applied to the spatial variations of radiance difference in a single image pair. Error is controlled in this sensitive measurement with narrowband filters, a low-noise infrared camera, and frame averaging. Averaging all image pixels reduces modeled and measured error to rmse $Q \cong 3.1$ W m^{-2}.

1. Introduction

Heat flowing between the ocean and atmosphere is affected by several well-measured geophysical parameters such as wind speed, air, and water temperature (Katsaros 1980). This flow is also affected by less well-measured parameters such as surface roughness, surface materials, and capillary–gravity waves (Fairall et al. 1996a). The relative contribution of each of these parameters on small scales ($<$1.0 m) must be accurately measured in order to accurately model air–sea thermal interactions on larger scales ($>$1 km). Estimating the relative contributions of these parameters to the total flux is a subject of ongoing research.

Since the current measurement methods for air–sea heat flux are valid over spatial scales that are relatively large compared to waves, it is especially difficult to isolate the contribution of capillary and gravity waves to total air–sea heat flux. All current heat flux measurements use parameters measured ''alongside'' the interface rather than at the interface itself. Relating these alongside parameters (air temperature, bulk water temperature, etc.) to a wave surface will require difficult measurements on time and space scales comparable to the wave.

A different approach is to measure the temperature gradient in the air–water interface. This interface is a bottleneck for heat flow because viscous surface effects force the heat to move by conduction rather than by eddy diffusion. Because of this conductive flow, the temperature gradient can be assumed to be linear for computational purposes (Katsaros 1980). Although this gradient is the ocean's largest thermal gradient, 0.2–0.6 K mm^{-1} (Katsaros et al. 1976), the depth over which a linear gradient occurs (the conduction zone) is small. The conduction zone thickness varies inversely with wind speed—approximately 1.0 mm in a calm zone, decreasing to 0.1 mm in the 1–5 m s^{-1} wind speed range, and finally being destroyed above approximately 8 m s^{-1} (Katsaros 1980). If this linear gradient can be measured, the heat flow can be calculated with Eq. 1:

$$Q = \kappa \frac{\Delta T}{\Delta z}, \tag{1}$$

where Q is the total heat flux, the sum of evaporative and sensible heat fluxes (W m^{-2}); κ is the thermal conductivity of water [6.09 mW/(cm K) at $T = 300$ K]; and $\Delta T/\Delta z$ is the temperature variation with depth (K cm^{-1}).

Previous attempts to measure the gradient used fine wire thermistors, which is a difficult technique because

Corresponding author address: Mr. Walt McKeown, Oceanography Division, RSA, Code 7340, Naval Research Laboratory, Stennis Space Center, MS 39529-5004.
E-mail: waltm@ltm.nrl.navy.mil

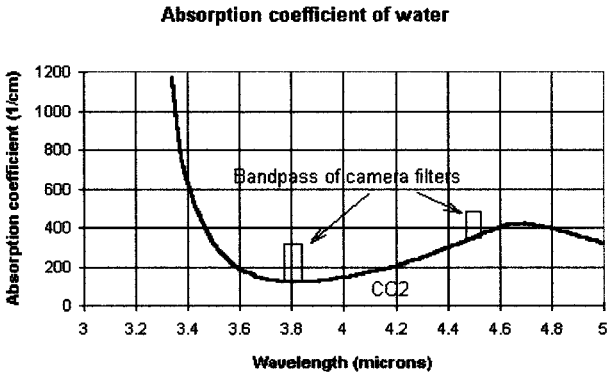

FIG. 1. Variation of water's absorption coefficient with a frequency of 3.5–5.0 microns (Wieliczka et al. 1989).

of the gradient's thinness and erratic motion (Mammen and von Bosse 1990). To avoid such difficulties, a remote sensing technique intended to measure heat flux variations over surface features has been developed. The technique relies upon the frequency variations in water's absorption coefficient, $\alpha(\lambda)$, caused by quantum molecular resonances. For water, $\alpha(\lambda)$ varies over seven orders of magnitude from the midinfrared to optical frequencies. Radiation at a frequency with a high absorption coefficient results from the skin temperature of the very topmost molecules. Radiation at a frequency with a lower absorption coefficient originates partly in the the top molecules and partly beneath the surface, inside the interface temperature gradient usually present just below the surface. The difference between these two radiances should vary with the interface gradient and also with air–sea heat flux. The relevant absorption coefficient variations are shown in Fig. 1.

This two-frequency approach originated in the late 1960s during the Barbados Oceanographic and Meteorological Experiment (McAlister and McLeish 1970). A temperature-calibrated instrument using 4.8 and 3.7 microns measured heat flux to within 10% of bulk surface measurements. While corrections for incidence angle and sea surface slope complicated the interpretation of the data, these effects should produce an error of less than 8% (Katsaros and Businger 1973). The detectors of the times limited further development of the technique. Over the last 30 years significant improvements have been made in infrared detectors and also bulk formula accuracy (Fairall et al. 1996b).

The interface temperature gradient can be measured in detail using interferometry in the 3.8-micron region (McKeown et al. 1995). A high spectral resolution instrument ($\lambda/\Delta\lambda = 1000$) produced an unprecedented vertical resolution of the interface gradient of about 10 microns. Since the passage of soluble gases through the interface is also constricted to diffusion processes, interferometric measurement of gas flux parameters using this gradient measurement has been proposed (McKeown and Asher 1997).

TABLE 1. Camera specifications.

FPA	Hybrid CCD/InSb
D*	8.4×10^{11} cm (Hz $W^{-1})^{1/2}$
Number of pixels	65 024 (256×254)
Pixel size	38 microns
Filter central frequencies	3.817 and 4.514 microns
Filter bandpass	0.1 micron
NEΔT	0.013 K (measured)
Lens	25 mm
View angle	37°

However, if a linear gradient can be assumed, it is not necessary to measure the entire gradient. Measurement at two points would be sufficient. If the two-frequency technique can be applied with a low-noise digital infrared camera, the result would be images in two frequencies with different absorption coefficients. This can be thought of as two temperature measurements on the linear gradient. Using the difference between the images, variations among the pixels would contain information about spatial variations of heat flux. A digital camera has two crucial advantages: averaging over all the image pixels or over many frames significantly reduces random noise. In addition, digital cameras use focal plane arrays (FPAs), an array of very small detectors on a chip at the camera's focal plane. Manipulation of this relatively large detecting area behind a camera's wide-angle lens can improve the signal-to-noise ratio (SNR) of this essentially weak signal.

To investigate this approach, a low-noise infrared camera was built by Amber Electronics (Goleta, California) and Infrared Laboratories (Tucson, Arizona) and used in the calibration and experiments described in section 3. The instrument cooled a filter wheel and an FPA of 256^2 pixels to 77 K with liquid nitrogen. Camera parameters are in Table 1.

Other researchers have employed near-IR cameras to examine waves in thermal detail intending to sense heat flux (Jessup et al. 1997; Jahne et al. 1989). Variations in radiometric sea surface temperature (RSST) on the order of 0.1–0.2 K were seen by Jessup and explained as convergence–divergence zones in the local water motion (Jessup et al. 1997). The experiments described here showed similar RSST spatial variations between the crest and trough of the 10-cm waves. The two-frequency approach differs from Jessup's in that a heat flux field rather than a temperature field is the goal. The desired information would not be in one thermal image but in the difference of two thermal images.

The heat flux technique developed by Jahne and others uses a laser to add heat to a point on the imaged wave surface (Jahne 1989). The time rate of change of the spot's temperature is thought to indicate thermal flow conditions in the interface. This information is then extrapolated to the rest of the wave image. The technique

outlined here differs from Jahne's in that it is passive, not active—no laser is required. Since the spatial variation of heat flow is the goal, the artificial addition of heat was rejected early on as a complication in the measurement.

For the two-frequency approach to be practical, one frequency must have a large absorption coefficient so that the radiation originates in the topmost molecules (T_{skin}). A number of infrared frequencies are suitable (Fig. 1); here 4.592 microns was chosen with $\alpha = 352.485\ cm^{-1}$ (Downing and Williams 1975). The other frequency must have a relatively small absorption coefficient to allow some of the radiation to originate inside the interface gradient. The lower the absorption coefficient, the more radiation from below the surface can emerge. The second frequency chosen for these experiments was 3.817 microns with $\alpha = 111.935\ cm^{-1}$ (Wieliczka et al. 1989). For instrument and noise reasons, it helps if the two frequencies are nearby. Spectral resolution in each case was $\lambda/\Delta\lambda = 38$, a bandwidth of 0.1 micron.

The two-frequency camera approach was explored at the Free Surface Hydrodynamics Facility, Naval Research Laboratory, Washington, D.C. during 1994–97. This paper presents the theory, a pure mathematical analysis, model and experimental results, and a discussion of potential field applications.

2. Theory

This measurement of air–sea heat flux (Q) requires the sensing of small radiance differences with frequency that are caused by variations in the interface temperature gradient. Radiance entering the camera is the sum of radiance leaving the water surface and upwelling atmospheric radiance. Radiance leaving the water is either emitted by water molecules or is reflected atmospheric radiance. The radiative transfer equation formalizes this approach. Frequency dependence (λ in microns) of all terms is implied. All temperatures are in degrees kelvin.

$$I = (1 - \varepsilon_{water})B(T_{air}) + \varepsilon_{air}B(T_{air}) + \varepsilon_{water}\int_0^\infty B[T(z)]\alpha e^{-\alpha z}\,dz, \quad (2)$$

where

- I = total radiance entering the camera (watts/m^2/micron/sr);
- ε_{air}, ε_{water} = emissivity of air and water, frequency dependent;
- $(1 - \varepsilon_{water})$ = reflection coefficient, frequency dependent;
- $B = c1/[\lambda(e^{c2/\lambda T} - 1)]$ = Planck radiation intensity [mW/(cm^2 − cm^{-1} sr)];
- T_{air} = air temperature, $T(z)$ = water temperature at depth z;
- T_{skin} = temperature of topmost molecules (K);
- α = absorption coefficient of water (cm^{-1}), frequency dependent; and
- $e^{-\alpha z}$ = water's transmittance over the depth z (cm), frequency dependent.

The first term represents radiation reflected off of the surface. This radiation can originate in the intervening atmosphere—from mirrors reflecting the water scene into the camera, the camera itself, the laboratory walls, ceiling, or support structures. Although the laboratory environment was temperature and humidity controlled and thus at the same temperature, various parts had different emissivities. Therefore, a hood was used over the experiments to eliminate nonuniform sources of reflected radiation. Since the source of reflected radiation was the same in all directions, a bidirectional reflectance function was not used. This term is minimized by a reflection correction during image acquisition and by the image differencing process. The air temperature used is that near the surface at surface pressure, which is the warmest in the air column. Using this conservative approach, the reflection terms were never found to be above the error from instrument noise or the regression relation.

The second term represents emitted atmospheric radiation going directly into the camera. This term is minimized by the short pathlengths (70 cm) and by the narrowband filter frequencies chosen for high atmospheric transmittance as well as water characteristics.

The third term in (2) represents radiation emitted by the water's temperature variations with depth, including the temperature of the topmost molecules T_{skin}. Radiation measured by the difference of two frequencies is represented by Eq. 3, which is the basis for modeling this technique:

$$I_{camera} = (\varepsilon_{3.8} - \varepsilon_{4.5})B(T_{air}) + \left\{\varepsilon_{4.5r}\int_0^\infty B[T(z)]\,d\tau_{4.5}\,dz - \varepsilon_{3.8r}\int_0^\infty B[T(z)]\,d\tau_{3.8}\,dz\right\}, \quad (3)$$

where I_{camera} is the total radiance entering the camera; $\varepsilon_{3.8}$, $\varepsilon_{4.5}$ are the emissivities of water at 3.8 and 4.5 microns, respectively; $\varepsilon_{3.8} = 0.977$; $\varepsilon_{4.5} = 0.98$; weighting functions are: $d\tau_{4.5} = \alpha_{4.5}e^{-\alpha_{4.5}z}\,dz$, $d\tau_{3.8} = \alpha_{3.8}e^{-\alpha_{3.8}z}\,dz$; and $\alpha_{3.8}$, $\alpha_{4.5}$ are the absorption coefficients at 3.8 and 4.5 microns.

Note that (1) and (3) describe the thermal conduction and radiative behavior of the same phenomena, but (1) does not appear in (3). The two equations are not formally linked until the $Q = f(\text{DADU})$ relationship is defined and measured in section 3a.

Each frequency's weighting function (Fig. 2a) indicates the percentage of total information arriving from each level in the water. The weighting functions for 3.8

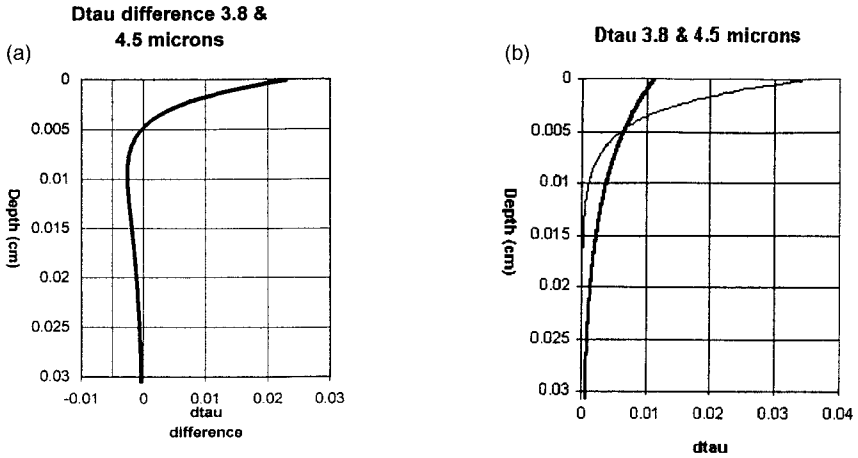

FIG. 2. (a) Weighting functions of 3.817 and 4.514 microns in water. (b) Differences of the weighting functions in (a).

microns indicate that some subsurface radiance information should emerge.

The weighting function difference (Fig. 2b) shows the source level of the radiation difference. Figure 2b indicates that information in an image difference originates in a zone centered on 0.01-cm depth. Since the conduction zone thickness varies with wind speed, the shallowness of this zone indicates this technique can work at wind speeds up to the threshold of about 8 m s^{-1} until the conduction zone is destroyed.

Although the radiance value in a pixel may contain heat flux information, the signal may be so small that the information cannot not be retrieved. Equation 3 was used to calculate the signal size for a representative range of heat flux values (Fig. 3). This calculation shows that rmse $\Delta T_b = 0.001$ K is equivalent to an rmse of approximately $\Delta Q = 10$ W m^{-2}. Achieving this level of accuracy in an absolute temperature measurement is unrealistic. Since a *relative* temperature difference is required here, this accuracy can be achieved using low-noise instruments with frame or pixel averaging.

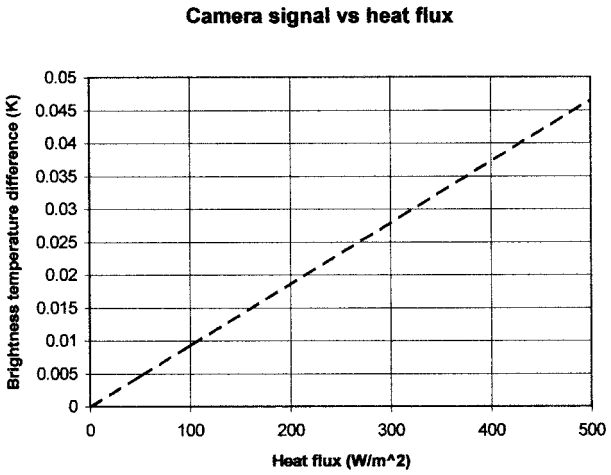

FIG. 3. Signal size vs heat flux from Eq. 3. Here, $\Delta T_b = 0.001$ K $\cong$ rmse $Q = 10$ W m^{-2}.

A brief calculation indicates this instrument using the two-frequency technique is capable of rmse $\Delta T_b = >0.001$ K. The instrument's tested NEΔT is 0.020 K, meaning that temperature changes below 0.020 K cannot be detected in one pixel. Calculation of the rmse ΔT_b for the difference of two images requires that these numbers be added quadratically. For the image difference, rmse $\Delta T_b = 0.028$ K. The calculations using (3), which are shown in Fig. 3, indicate that this error is equivalent to rmse $Q = \sim 280$ W m^{-2}. However, averaging over all the pixels in a 256 $\times$ 256 image reduces this by a factor of 256, resulting in rmse $Q = 1.09$ W m^{-2}. If NEΔT = 0.050 K, rmse $Q = 7.07$ W m^{-2}. Such low-noise performance is commercially available in arrays larger than 256^2. These values agree numerically with the independent analysis of section 2a.

Therefore, the instrument is capable of sensing the small T_b differences required if all image difference pixels are averaged. Although the image is lost, these pixel-averaged values can be used to determine the regression relationship between DADU and heat flux Q. Regression coefficients determined in this way are ''robust'' and noise resistant, which are effects employed in the technique described here. Depending on the desired products, field use may require frame averaging rather than pixel averaging (section 4b). Judicious use of frame or pixel averaging can improve the measurement accuracy several orders of magnitude, which is sufficient for these purposes. Measurement error is covered in detail in section 3d.

a. Mathematical analysis

This analysis addresses the following question: Can the heat flux through an air–water interface be determined from two radiometric temperature measure-

ments? It is assumed that the optical properties of water are well known, that losses due to atmospheric absorption are negligible (short pathlength), and that the radiation is collimated.

The water temperature profile at and near the interface can be described as a linear function of depth:

$$T(z) = T_{\text{skin}} + \left.\frac{\partial T}{\partial z}\right|_0 z, \tag{4}$$

where $(\partial T/\partial z)|_0$ is an unknown physical surface temperature gradient.

If the absorption coefficient is sufficiently high, (4) has two unknowns: skin temperature and the subsurface temperature gradient.

Radiance in terms of measured brightness temperature is defined as

$$B[\lambda, T_b(\lambda)] = \frac{2hc^2}{\lambda^5\left[\exp\left(\frac{hc}{\lambda k T_b(\lambda)}\right) - 1\right]}, \tag{5}$$

where λ is the wavelength (cm); h is Planck's constant (erg s); c is the speed of light (cm s^{-1}); and k is Boltzmann's constant (erg K^{-1}).

Substituting the temperature profile into the radiative transfer equation (2), we can relate an unknown temperature profile to the emitted radiation at each frequency λ:

$$B[\lambda, T(z)] = \int_{-\infty}^{0} \frac{2hc^2}{\lambda^5\left[\exp\left(\frac{hc}{\lambda k T(z)}\right) - 1\right]} \alpha e^{\alpha z}\, dz. \tag{6}$$

If a linear temperature gradient is assumed, then

$$\frac{2hc^2}{\lambda^5\left[\exp\left(\frac{hc}{\lambda k T_b(\lambda)}\right) - 1\right]} \approx \frac{1}{\alpha_\lambda + \frac{hc}{\lambda k}\frac{1}{T_{\text{skin}}^2}\left.\frac{\partial T}{\partial z}\right|_0}\left(\frac{2\alpha_\lambda hc^2}{\lambda^5\left(\exp\frac{hc}{\lambda k T_{\text{skin}}}\right)}\right). \tag{7}$$

There are now two unknowns and two equations (one in each frequency):

$$T_b(3.8\ \mu), T_b(4.5\ \mu) \rightarrow T_{\text{skin}}\left.\frac{\partial T}{\partial z}\right|_0. \tag{8}$$

Solving for T_{skin} yields

$$T_{\text{skin}} = \frac{\left(\frac{1}{\lambda_{4.5}} + \frac{1}{\lambda_{3.8}}\right)}{\left\{\Omega + \left[\frac{1}{\lambda_{4.5} T_{b(3.8)}} - \frac{1}{\lambda_{3.8} T_{b(4.5)}}\right]\right\}}, \tag{9}$$

where

$$\Omega = \left(\frac{k}{hc}\right)[\ln(\lambda_{4.5}\alpha_{4.5}) - \ln(\lambda_{3.8}\alpha_{3.8}) + \ln(\lambda_{3.8}\alpha_{3.8} - \lambda_{4.5}\alpha_{4.5})].$$

Solving for $(\partial T/\partial z)|_0$ gives

$$\left.\frac{\partial T}{\partial z}\right|_0 = \left(\frac{k}{hc}\right) T_{\text{skin}}^2 \lambda_{3.8}\alpha_{3.8} \times \left[\exp\left(\frac{hc}{k\lambda_{3.8}}\right)\left(\frac{1}{T_{b(3.8)}}\right)\left(\frac{1}{T_{\text{skin}}}\right) - 1\right]. \tag{10}$$

Since all the parameters on the right-hand sides of (9) and (10) are either well known or accurately measured, the skin temperature and the temperature gradient can be determined by two radiometric measurements. While this analysis ignores some details (reflected radiation and apparent emissivity), it correctly describes the major features.

b. Model

A mathematical model based on (3) was constructed to verify experimental observations and identify error sources. Model inputs are water temperature and heat flux. Model outputs are electrons per measurement and measurement error. Electrons per measurement is linearly related to the camera output of analog-to-digital units (ADU). This relationship encodes the camera settings of gain, offset, frame rate, and integration time, which are optimized for the environmental conditions.

The assumptions in the model were that a conduction zone exists where the temperature gradient is linear, that no effects due to surface materials exist, and that the surface is flat.

The camera system was characterized by the optical field of view (FOV), optical losses (filter, lens, bounce mirror), out-of-band transmission (photon leakage in the filter), dark current, read noise, and throughput. The water was characterized by the real and imaginary parts of the refractive index, which were used to calculate emissivity and absorption coefficient in each frequency (Wieliczka et al. 1989). Radiance arising from the water was calculated with (3). The interface temperature gradient was calculated from a formula derived from the thermal conduction formula:

$$Q = \kappa T(z) \ggg T(z) = \frac{Qz}{\kappa} + T_{\text{skin}}. \tag{11}$$

The model calculated error from reflection (caused by emissivity variation with frequency), atmospheric absorption (transmittance variation with frequency), and quantum noise. The outputs behaved like the experiment's outputs and indicated a measurement error from the camera system of less than 1 W m^{-2}.

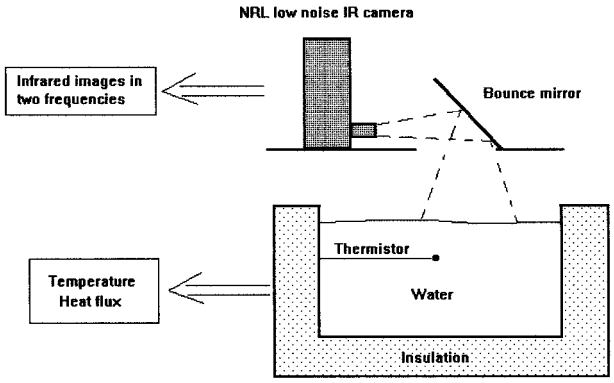

FIG. 4. Experimental configuration.

3. Experiment

To test these conclusions, experiments were conducted at the Naval Research Laboratory's Free Surface Hydrodynamics Laboratory. The experimental configuration is shown in Fig. 4.

A typical experiment began by warming the water mass several degrees Celsius above air temperature (T_{air} = 19°C) and then allowing it to cool to room temperature. This is the heat flux calibration phase used to determine the $Q = f(\text{DADU})$ relationship. During each minute of the cool-down phase (several hours), the camera takes 200 images at 3.817 microns and 800 images at 4.514 microns. The mean of the average of these images in each frequency was recorded. Water temperature, supplied by thermistors embedded in the water mass, is also recorded. The rate of change of temperature with time of a well-known water mass (corrected for imperfect insulation) allows calculation of heat flowing through the interface. A weak wind (<0.1 m s^{-1}) was applied to draw away the evaporated water and to induce a slight circulation, which minimized thermoclines.

The difference of each image's ADU values gave DADU variation with time. Combined with heat flux from the thermistors $Q(t)$, this allows calculation of the Q(DADU) relationship.

After covering a range of several degrees kelvin and several hundred W m^{-2}, the water was rewarmed to the midpoint of the temperature range and a simple paddle-type wavemaker (not shown in Fig. 4) was activated. As the wave moved across the tank, an image sequence was taken in each frequency. From these sequences, an image in each frequency was chosen in which the wave crest was in an identical position. These images were then subtracted to produce a DADU image of the wave. This was converted to a Q map using (15).

a. Heat flux calibration

Infrared measurements are normally calibrated with temperature to determine the relationship between radiance (B) and camera output (ADU). This relationship is $B = f(\text{ADU})$. A calibration body supplies the known radiance. When using image differences, the subtraction of ADU from two images (DADU) requires a radiance–DADU relationship to be known [$B = f(\text{DADU})$].

Seeking such small signals as these requires a reevaluation of all error sources. Calibration errors can result from imperfectly known blackbody radiance parameters (temperature, emissivity), unknown temperature gradients on the face of the calibration body, or slight temperature changes over the time spent calibrating. When sensing heat flux, calibration errors can easily approximate the size of the signal ($\sim$0.01 K equivalent to $\sim$100 W m^{-2}). Since sensing heat flux is the objective here, thermal calibration error was avoided by calibrating the camera's DADU with heat flux to determine the relationship between Q and DADU [$Q = f(\text{DADU})$].

Since the wide variety of camera settings affect ADU, the $Q = f(\text{DADU})$ relationship is unique to each combination of gain, offset, integration time, and frame rate as well as the camera system. In practice, these settings were chosen to maximize the camera's sensitivity to small radiance differences between channels. Heat flux calibration uses the same water, lenses, pathlength, reflection, etc., as does the measurement. Any unknown errors from these sources are incorporated into the calibration coefficients and minimized.

Since the same DADU values may represent a range of heat flux values depending on camera settings, the settings and the $Q = f(\text{DADU})$ relationship were determined before waves were imaged. A range of heat flux values was generated by letting water change temperature in a well-insulated tank (Fig. 4). The cool-down phase (temperature change with time of the water mass) allowed the heat loss over time [$Q(t)$] through the interface to be measured. The camera automatically recorded 800 images every minute: 600 images at 4.5 microns and 200 images at 3.8 microns. Including the filter change, this total acquisition took 20 s. Each image sequence was averaged and corrected for background variations. The usual 6-h run produced 3×10^6 images to be averaged to determine DADU(t). Plotting Q(t) versus DADU(t) allows a regression relationship to be determined (Fig. 5).

To determine the $Q = f(\text{DADU})$ relation, it is assumed that the following is true:

$$Q = \Gamma(\text{DADU}), \tag{12}$$

where Γ is an unknown function of camera parameters, temperature, and heat flux.

A regression curve is then fit between heat flux and the DADU data plotted in Fig. 5, which takes the form

$$Q = \alpha - \beta(\text{DADU}) + \chi(\text{DADU}^{-2}), \tag{13}$$

where Q is the total heat flux (W m^{-2}). For the example shown, $\alpha = 18\,083$, $\beta = 30.615$, and $\chi = 0.013063$.

This approach works well in the laboratory where the water conditions are well controlled. For field use, a ''field calibration'' approach is outlined in section 4d.

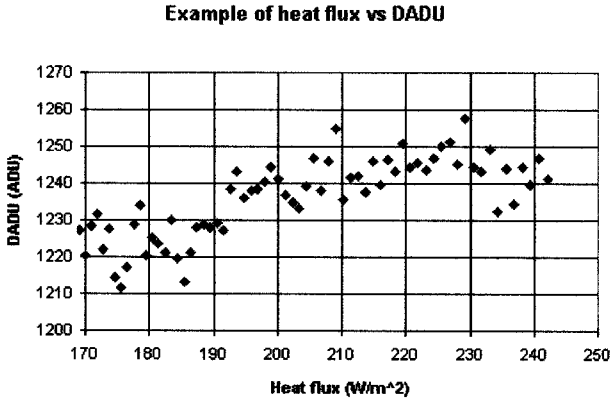

FIG. 5. Example of data used to calculate a $Q = f(\text{DADU})$ relationship. Each point is the average of the spatial averages of 800 images. Heat flux is measured independently. The tank did not cool down evenly over time but showed weak variations in cool-down rate due to internal flow changes. This tank ''surging'' caused some of the scatter.

b. Relative contributions of temperature and heat flux

Since both temperature (T) and heat flux (Q) changed simultaneously in these experiments, their relative contribution to the total change in DADU (ΔDADU) must be determined. Here, T and Q were the only parameters changing; therefore, ΔDADU must be caused by the sum of the changes caused by each parameter.

$$\text{If} \quad \text{DADU} = f(T, Q),$$

then

$$\Delta\text{DADU} = \left(\frac{\partial\text{DADU}}{\partial T}\right)_Q dT + \left(\frac{\partial\text{DADU}}{\partial Q}\right)_{\text{Temp}} dQ, \quad (14)$$

where ΔDADU is the total change in DADU over time or space, $(\partial\text{DADU}/\partial T)_Q$ is the change of DADU with temperature while heat flux is constant, and $(\partial\text{DADU}/\partial Q)_{\text{Temp}}$ is the change of DADU with heat flux while temperature is constant.

These terms were measured during two parallel experiments that were identical in all respects (camera settings, surface area, pathlength, range of T and Q) except for slight (1%) differences in water mass. This mass difference caused the water to lose heat at a slightly different rate during the cool-down phase, subsequently causing two different heat fluxes at any one temperature and two different temperatures at any one heat flux.

This process generated two sets of data pairs. One set consisted of data pairs that had temperature in common but different heat fluxes (Fig. 6a). The other set consisted of data pairs with heat fluxes in common but different temperatures (Fig. 6b). These datasets were combined to evaluate the terms in (14).

The temperature contribution to DADU change (14, first term) was 97.3% of the total change. The heat flux contribution to DADU change (14, second term) was 2.7%. These values derived from experiment are very close to the model's radiation response for the same experimental conditions.

Since DADU is a function of just two parameters, the contribution of both parameters need not be calculated. After one parameter's contribution is determined, the remainder can be assigned to the second. This would not be the case if three or more parameters were changing DADU. This means that the dT contribution need not be determined and, in effect, eliminates the need for a temperature calibration.

The small size of the heat flux contribution (2.7%) is not surprising, considering the weighting functions (Fig. 2). What is important is that this number is well known. The SNR (SNR = 1180) indicates that the second term of (7) is known to 1 part in 31.54, an error equivalent to 2.51 W m^{-2} over this range of Q and T.

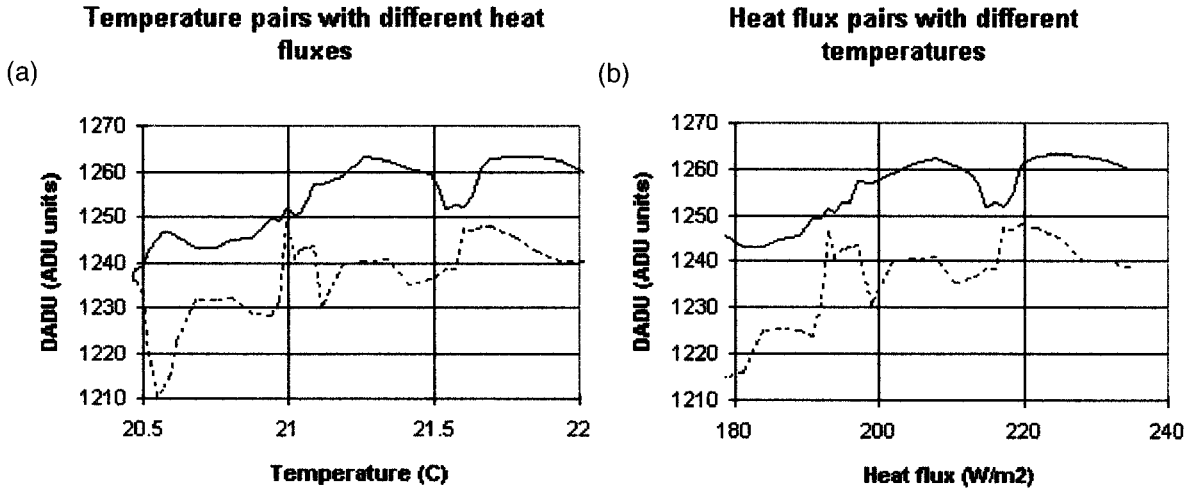

FIG. 6. The combined camera response from two experiments that cooled down slightly different water masses. The mass difference caused different cool-down rates. (a) Data pairs that had the same heat flux at different temperatures. (b) Data pairs that had the same temperature at difference heat fluxes. Total of 7000 images.

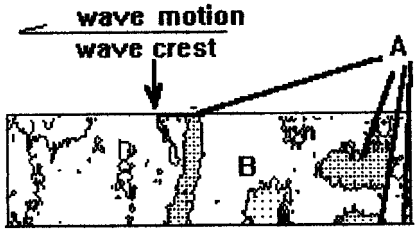

FIG. 7. Contour map of heat flux variations on a 10-cm wave. Footprint size 53.3 cm × 53.7 cm. Spatial resolution is 2.1 mm. Here, rmse is 3.1 W m^{-2}. Text refers to areas marked A and B.

The Q contribution was determined relative to time but can be applied relative to time or space here. Since determination of the $Q = f(\text{DADU})$ relationship used the mean image DADU, and since the independent heat flux measurement was also the mean image value, variations of DADU over the image can be ''anchored'' at the mean DADU. The mean Q (measured independently) is assigned to the pixel with this value. The Q in any other pixel can then be calculated from the derivative of (13):

$$Q_{\text{pixel}}(x, y, \text{DADU}) = \overline{Q}\,[\overline{\text{DADU}}\,(x_0, y_0)] + \sigma\Delta\text{DADU}(x, y), \quad (15)$$

where Q_{pixel} is a pixel's heat flux value at image position (x, y); $\overline{Q}(\overline{\text{DADU}}, x_0, y_0)$ is the mean heat flux value at the mean DADU pixel at image position (x_0, y_0), which is the zero point of Cartesian image coordinates; σ is the percentage of DADU variation due to heat flux variation (2.7% for this example); and α, β, χ are the coefficients in Eq. 13. Here $\Delta\text{DADU}(x, y)$ is the difference of DADU at (x, y) from the mean DADU at (x_0, y_0), which equals

$$(\beta + 2\chi\text{DADU})\frac{d\text{DADU}}{dx, dy}. \quad (16)$$

In this way, a heat flux value is extracted from each pixel's DADU value, mapping the heat flux variations over the surface.

Since the camera's response is linear to photon counts and nonlinear to radiation, the effect of the temperature difference over the wave can be ignored because this temperature difference is small (typically <0.2 K). In addition, the Q(DADU) relationship was determined over a temperature and heat flux range (typically 2.0 K and 200 W m^{-2}), which includes the wave values of those parameters. In other words, the wave images were taken under the same conditions as the calibration, which is a consequence of laboratory conditions. Field use will require the temperature range over the wave be determined. The modified algorithm for field use is explained in section 4d.

c. Results

The Q map (Fig. 7) and Q profile (Fig. 8) are the result of this process. Although all data are produced by a thermal imager, spatial variations of temperature and heat flux differed in details. This indicates that spatial variations of the radiance difference are different than the spatial variations of each channel's radiance. The means of the Q map and Q profile also match the heat flux values measured independently by thermistors. These spatial averages and spatial variations are the only validation possible; fine-wire probes into a single pixel's temperature gradient are impractical under these conditions but may possibly be included in more advanced experiments using ''two-camera'' or ''two-color'' instrumentation (explained in section 4c).

The interface ahead (left) of the wave (Figs. 7 and 8) was undergoing the slow overturning motion typical of surface renewal. The wave crest distorted these characteristically weak thermal features during passage. Semiregular features with axes parallel to the wave mo-

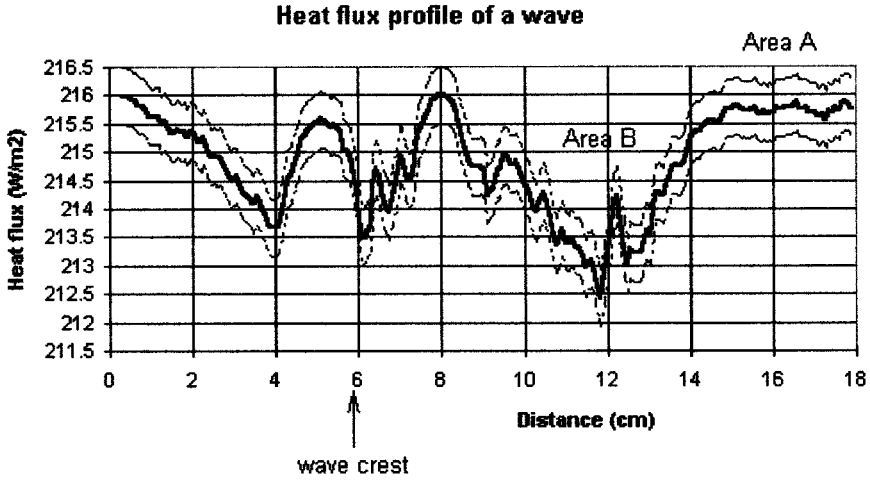

FIG. 8. Heat flux profile over a small wave. Here, Q values are derived from the modified $Q = f(\text{DADU})$ relationship and are the area averages in Fig. 7a. Error bars are 1 W m^{-2}.

tion (area ''A'' in Fig. 7) show up behind the crest. The (assumed) thinning of the conduction zone at the crest is repeated here due to subsurface vorticity. The area marked ''B'' in Fig. 7 is a low flux zone where the conduction zone temporarily thickened. The net effect is that the wave seems to ''comb'' the surface renewal features into temporary parallel rows before surface renewal motion dominates once again farther downstream.

The wave crest is cooler with lower heat flux. It is assumed that this occurs because the conduction zone is thickest where the interface has the highest curvature. The high heat flux ahead and especially just behind the crest results from a stretching of the ambient conduction zone as the wave passes. The lines placed elsewhere on the Q map may show different details, but the basic features of this complex process remain and move with the wave: high heat flux in the trough, low heat flux at the crest.

These results are not intended to explain the near-surface hydrodynamics of wave features but simply to illustrate the technique's use. More precisely calibrated waves combined with particle image velocimetry techniques are required to study the hydrodynamic causes of temperature and heat flux patterns. Depending on the characteristic feature size of the phenomena to be studied, larger footprints and/or different spatial resolutions will result from using different pathlengths and lens focal lengths. For example, instead of the wide-angle 37° FOV lens and 60-cm pathlength used here (spatial resolution ~2 mm), a narrow FOV lens and shorter pathlengths should result in spatial resolutions below 0.5 mm. The narrower solid angle would decrease the SNR proportionally to the ratio of the current/proposed solid angles in steradians.

d. Discussion

Treatment of the major measurement error sources is outlined in Table 2. The laboratory atmosphere was filtered and enjoyed well-controlled temperature and humidity (~1.0-K temperature and 2.0-K dewpoint temperature). The camera was enclosed to eliminate wind effects on the camera casing from the atmospheric control blowers. The lens was stabilized against temperature changes from air temperature variations by using a flow-through water jacket. Double filters in each channel eliminated out-of-band photons (radiation from outside the filter's bandpass limits) down to 10^{-6} of the in-band radiation. The model indicates that doubling removes out-of-band photons from causing significant error. The effect of surfactants was minimized by tank scrubbing before and after each experiment, a downwind collection beach, and other measures. All mirrors were first surface mirrors to minimize reflectance losses. A black cloth shroud over the experiment ensured that the photons from reflection entering the detector arose from a directionally uniform source (the cloth) rather than local hot spots (lights, hot water pipes, etc.).

TABLE 2: Sources of measurement error, the treatment for minimization, the relevant parameter, and the resulting numerical value (W m^{-2}).

Error type	Treatment	Relevant parameter	Result (W m^{-2})
Background	Corrected during experiment	ΔDADU/pixel	0.01
Calibration	$Q = \frac{\frac{\Delta T}{\Delta t} C_p \mathrm{Vol} \rho}{A}$	T error = 0.01 K	0.02
Regression	Correlation coefficient 0.97703 (3 min smoothing)		3.1
System bias	Channel subtraction	Bias = ~0.01 K per channel	~0.1
System and quantum noise	Frame averaging	1000 frames	1.011

The image differencing central to this technique minimizes many error sources common to absolute infrared measurements. Reflection error dropped because reflection coefficients used in the first term of (2) are reduced in the first term of (3) from 0.02 to 0.004. Similar reductions occur for errors arising from atmospheric transmittance, background radiation variations, and filter emissivity. System bias (ADU values added to or subtracted from the signal and arising from the total camera system) is minimized by differencing. Lens emissivity errors dropped 0.07–0.0049. Errors from quantum noise were minimized by averaging 800 frames each minute for 6 h for the regression analysis.

Background corrections were applied while the images were saved. The background image used was a 100-frame average of the flat water taken over a 5-min interval to average out thermal surface renewal features. Calibration error is small because temperature and water mass are very well known (0.01 K and 0.02 mL, respectively). Each frequency's image was calibrated before and after an experiment with a thermally controlled cavity having a thermal stability of 0.03 K (Gasparovic and Tubbs 1975). The major source of error arises from the regression relationship $Q = f(\mathrm{DADU})$.

When two images are taken with one camera, image blurring is unavoidable. Changing filters and saving the images on disk requires a few seconds, so the wave has moved out of the image. This meant that two identical waves must be generated, one for imaging in each frequency. While the resulting waves were nearly identical on the scale of the wavelength (10 cm), the waves were not identical on the scale of the spatial resolution of the images (2 mm). When the two images are subtracted, blurring occurs. This source of blurring can be eliminated by the two-color or two-camera designs outlined in section 4c.

Since temperature and heat flux were changing slowly during the time required to change filters and acquire

the second wave's image sequence, the effect of wave-to-wave variability on the measurement was examined. The water mass of about 50 gal was large enough to make the time rate of change of these parameters slow. During a typical experiment with realistic ocean heat fluxes, these values were $\Delta T_{\text{water}} = 0.0012$ K min^{-1} and $\Delta Q = 0.0504$ W m^{-2} min^{-1}. Since waves were imaged in each frequency within the same minute—wave-to-wave variability in heat flux is much lower than the approximate 1.0–3.0 W m^{-2} of the measurement—this effect is discounted. As for temperature, the rate of 0.0012 K min^{-1} approaches significance because the signal of $\Delta T_b = 0.001$ K is equivalent to 10.0 W m^{-2} (section 2b). However, the brightness temperature of both channels is changing with the water temperature. This brightness temperature difference is the essence of the measurement. The time rate of change of this difference is an order of magnitude smaller than water temperature changes: $\Delta T_{b_{\text{water}}} = \sim 0.0001$ K min^{-1}. Using (3) in the model as outlined in section 2b, this change of brightness temperature difference with time is slightly less than the error from regression ($\sim$1.0 W m^{-2}). A two-camera or two-color system would also eliminate this source of error because the images would be taken on a single wave simultaneously.

Averaging groups of pixels in one image increases accuracy but degrades the spatial resolution. If high spatial resolution is required, frame averaging is preferred. Appropriate closed-cycle cameras (no liquid nitrogen required), with NEΔT = 0.020 K and capable of 1400 Hz, are commercially available. Averaging 1.0 s of such data (1400 frames) reduces noise by a factor of 37, equivalent in Fig. 7 to rmse $<$8.0 W m^{-2}. The surface feature must be fixed in the image plane, either by moving the instrument with the feature or reregistering an image sequence during postprocessing.

Theory thus indicates the radiation difference caused by the interface temperature gradient ($\Delta T_b = 0.001$ K) can be sensed using current instrumentation and techniques.

4. Field use

The authors fully appreciate the transition difficulties moving a measurement from the laboratory to the field. This technique is not field ready. Further testing with redesigned instrumentation is essential before attempting to map an ocean wave's heat flux patterns. This section discusses potential difficulties, use strategies, and field calibration.

a. Constraints

Night use is clearly required because solar reflection will swamp the signal. Wind speeds below about 8–10 m s^{-1} are required because the linear gradient assumption fails when breaking waves rupture the interface.

The camera(s) must be low noise (NEΔT $<$ 0.020 K) so that the small signal will emerge in the image difference. The camera system must be fast ($>$1000 Hz) because the time required for the total sequence must be small compared to the phenomena's characteristic time.

Simultaneity (both images produced simultaneously) should be inherent in a field camera. Simultaneity eliminates blurring (section 3d); there should also be a restriction to stationary or periodic phenomena. Any surface feature becomes suitable for mapping: Langmuir cells, ocean fronts, capillary or gravity waves, ship wakes, etc.

Both images must be collocated so that corresponding pixels from the two images perfectly overlap. In two-lens systems designed for collocation, the optical problems arise primarily from slight differences between lenses. The camera designs (section 4c) vary the FPA but use one lens.

A suitable platform may be a ship, viewing forward from a slowly moving helicopter, or a light, low-altitude aircraft, depending on the desired product. Footprint size will vary with altitude; for the current system with a 37° FOV lens, the footprint is 0.68 times the aircraft altitude.

Reflection error must be considered because even a clear night sky radiating at about 250 K will cause a $\Delta T = 0.05$ K between the two frequencies. Reflection error can be minimized by measuring downwelling radiation with the camera itself. Imaging vertically upward with a bounce mirror gives a measurement useful in place of $B(T_{\text{air}})$ in the first term of (3). This minimizes reflection error if the night sky is uniform (all clear or all cloudy). If partial cloudiness exists, the unknown wave slope in each pixel can induce local areas in the image with slightly anomalous values. This might be treatable with smoothing filters that spread the error over many pixels.

Atmospheric transmittance error, arising from unknown channel differences in absorption, may become significant over long distances and can be minimized in several ways. Calibrating at the distances to be used in the field is recommended. If this is not feasible, an atmospheric model (FASCODE, MODTRAN) coupled with accurate pathlength measurements (radar altimeter or laser range finder) will allow the atmospheric transmittance values to be well determined and compensated for. Knowledge of the boundary layer's temperature and moisture profile can also be acquired with thermistor strings, dropsondes, for aircraft altitude changes, again using an atmospheric model to compensate.

b. Products and use strategy

Two different products may be sought: ''mapping'' or ''spot'' measurements. Mapping (producing heat flux contour maps of a feature) is the more difficult product, requiring trained use of specialized instrumentation and postprocessing. Spot measurements (producing one heat

flux value averaged over the footprint) are relatively easy to do, have the highest possible accuracy, and require little postprocessing, but no image results. Different approaches are required for these two products.

Spot measurements are produced by averaging the measurement over all image pixels. Random noise is reduced by a factor that is the square root of the number of pixels. Since the present camera has 256^2 pixels, noise is reduced two orders of magnitude this way. Larger FPAs currently number above 1000^2. This approach requires little postprocessing and should be feasible from low-flying aircraft. Spacing along the flight path will depend upon aircraft and camera speed. The current system, using an automated filter wheel on one 60-Hz camera, could make 10 heat flux measurements per minute along a flight path. A digital frame-grabber card would increase this to about 60 measurements per minute. Finer spacing will require a faster camera or a slower airplane.

Mapping is designed to produce heat flux maps on actual ocean waves. Several constraints appear because of this requirement. Since the pixel averaging degrades the image's spatial resolution, frame averaging must be the primary noise reduction strategy. Frame averaging requires that the surface feature remain stationary in the image if the feature's details are to be preserved. For a wave moving relative to the camera, this can be done by quickly taking an image sequence with a fast (>1000-Hz camera) and reregistering the images during postprocessing. It is inevitable that the feature's image position will move slightly during the sequence. The image sequence can later be reregistered on common details (crest, bubble patterns, foam patch, etc.) in image coordinates. Correct postprocessing will cause the wave to appear stationary during the sequence. The average of each pixel's DADU in the sequence then contains the heat flux information for processing.

c. Instrument design

While the current one-camera, two-image system is adequate for spot measurements, a more versatile system is needed for mapping. Both images must be rapidly acquired simultaneously and with collocated footprints.

Speed is required to reduce the time needed to acquire sufficient noise-suppression frames relative to the phenomena's characteristic time (for waves, ~1 s). For example, a coregistered sequence of 1000 frames acquired using a 1000-Hz frame rate reduces random noise by a factor of 31. Compared to the noise reduction of 256 in spot averaging, this is barely sufficient to bring rmse $Q < 10$ W m^{-2} in mapping. A careful operator with a flexibly mounted camera can probably stretch this out for 5+ s to approach rmse $Q = 5.0$ W m^{-2}. The actual spatial variations of heat flux associated with an ocean wave are currently unknown.

Several camera designs are suggested for mapping a wave's heat flux patterns (Figs. 9a,b). The first is a two-FPA system (Fig. 9a): two filtered FPAs sensing through a beamsplitter, all in one dewar. Another design uses a two-color camera (Fig. 9b): one FPA constructed so that each frequency is measured simultaneously without filters. Such detectors are just becoming available.

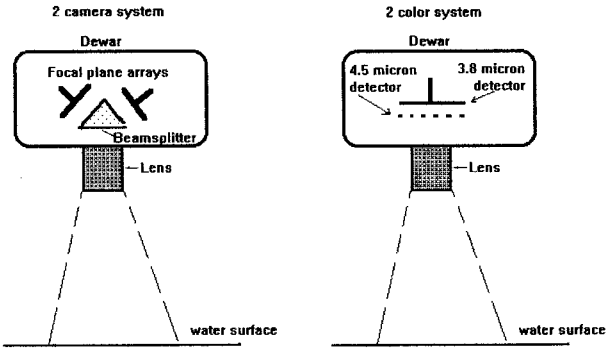

FIG. 9. Schematic of a (a) two-camera system and a (b) two-color system.

d. Field calibration

Since field conditions are not well controlled, a field calibration technique is suggested here to eliminate any skin temperature dependence of (13), (14), and (15) in the measurement. In effect, field calibration constructs a look-up table ADU and Q values that allow calculation of these equations for any skin temperature over a range of heat fluxes. Since the $Q = f(\text{DADU})$ relation is strongly affected by camera settings, the optima settings must be determined before any calibration is performed.

In a field calibration, the physical process outlined in section 3b is repeated a number of times. Between each run, a small amount of the water mass (<1%) is added or removed. Each run covers the range of temperatures and heat fluxes expected in the field. This process is repeated until the dataset is sufficiently large so as to fully determine the relative contributions of temperature and heat flux to the signal at any observed ADU(4.5). It will not be difficult to acquire a sufficiently large dataset with a fast camera. From these data, the $Q = f(\text{DADU})$ relationship for any ADU(4.5) can be determined.

Skin temperature and ADU(4.5) are considered equivalent here because the 4.5-micron channel has a high absorption coefficient and so responds almost exclusively to skin temperature, not heat flux. The relation between skin temperature and ADU(4.5) can be quantified by a standard thermal calibration with a blackbody.

The data from field calibration is of the form

$$P(t) = \overline{\text{ADU4.5}(t)}, \overline{\text{ADU3.8}(t)}, \overline{\text{DADU}(t)}, \overline{Q(T_{\text{water}}, t)}, \quad (17)$$

where $P(t)$ are the data values coincident at any time t. Here, $\overline{\text{ADU4.5}(t)}$, $\overline{\text{ADU3.8}(t)}$ are the mean ADU values

in the 4.5- and 3.8-micron frequencies averaged over a sufficient number of frames and/or pixels to minimize random variations and measured coincident in time with $Q(T_{water}, t)$. Also, $\overline{\text{DADU}(t)} = \overline{\text{ADU4.5}(t)} - \overline{\text{ADU3.8}(t)}$ are mean DADU values and $\overline{Q(T_{water}, t)}$ is mean heat flux determined by the time rate of change of the bulk water temperature (as determined by thermistors) and measured coincident in time with the camera measurements that determine $\overline{\text{ADU4.5}(t)}$ and $\overline{\text{ADU3.8}(t)}$.

Field calibration using a fast, flexibly mounted two-FPA or two-color system at field distances will produce a look-up table to allow remote sensing of heat flux in either spot or mapping modes from the appropriate platform.

5. Conclusions

An infrared camera technique designed to measure air–water heat flux has been developed. This remote sensing technique is based on the radiance difference between two frequencies in which water's absorption properties differ. Feasibility is supported by modeling studies, laboratory experiments, and mathematical analysis. In the laboratory, the technique is suitable for stationary or reproducible periodic phenomena (waves) using the present one-camera system. Field use will require a more specialized two-FPA or two-color camera system to minimize random noise errors. When all image pixels are averaged, the measurement error from random noise drops to rmse $Q = \sim 1.0$ W m^2 in both model and measurements. This indicates that accurate remote sensing of air–sea heat flux is feasible using suitable techniques and instrumentation. The effects of surfactants, aerosols, and wave slope variations were not included in this analysis.

Acknowledgments. Walt McKeown was supported by the National Research Council Associateship program during the time this work was completed.

REFERENCES

Downing, H. D., and D. Williams, 1975: Optical constants of water in the infrared. *J. Geophys. Res.,* **80,** 1656–1661.

Fairall, C. W., E. F. Bradley, J. S. Godfrey, G. A. Wick, J. B. Edson, and G. S. Young, 1996a: Cool-skin and warm-layer effects on sea surface temperature. *J. Geophys. Res.,* **101** (C1), 1295–1308.

——, ——, D. P. Rogers, J. B. Edson, and G. S. Young, 1996b: Bulk parameterization of air/sea fluxes for Tropical Ocean-Global Atmosphere Coupled Ocean–Atmosphere Response Experiment. *J. Geophys. Res.,* **101** (C2), 3747–3764.

Gasparovic, R. F., and L. D. Tubbs, 1975: Influence of reference source properties on ocean heat flux determination with two-wavelength radiometry. *J. Geophys. Res.,* **80,** 2667–2671.

Jahne, B., P. Libner, R. Fischer, T. Billen, and E. J. Plate, 1989: Investigating the transfer processes across the free aqueous boundary layer by the controlled flux method. *Tellus,* **41B,** 177–195.

Jessup, A. T., C. J. Zappa, and H. H. Yeh, 1997: Defining and quantifying microscale wave breaking with infrared imagery. *J. Geophys. Res.,* **102** (C10), 23 145–23 153.

Katsaros, K. B., 1980: The aqueous thermal boundary layer. *Bound.-Layer Meteor.,* **18,** 107–127.

——, and J. Businger, 1973: Comments on the determination of the total heat flux from the sea with a two-wavelength radiometer system as developed by McAlister. *J. Geophys. Res.,* **78** (12), 1964–1969.

——, W. T. Liu, J. A. Businger, and J. E. Tillman, 1976: Heat transport and thermal structure in the interfacial boundary layer measured in an open tank of water in turbulent free convection. *J. Fluid Mech.,* **83,** 311–335.

Mammen, T. C., and N. von Bosse, 1990: STEP—A temperature profiler for measuring the oceanic thermal boundary layer at the ocean–air interface. *J. Atmos. Oceanic Technol.,* **7,** 312–322.

——, and ——, 1970: A radiometric system for airborne measurements of the total heat flow from the sea. *Appl. Opt.,* **9,** 2697–2705.

McKeown, W., and W. Asher, 1997: A radiometric method to measure the concentration boundary layer thickness at an air–water interface. *J. Atmos. Oceanic Technol.,* **14,** 1494–1501.

——, F. Bretherton, H. L. Huang, W. L. Smith, and H. L. Revercomb, 1995: Sounding the skin of water: Sensing air/water interface temperature gradients with interferometry. *J. Atmos. Oceanic Technol.,* **12,** 1313–1327.

Wieliczka, D. M., S. Weng, and M. R. Querry, 1989: Optical constants of water in the infrared. *Appl. Opt.,* **28,** 1714–1719.